

Supporting Information

Ultrastretchable Conductive Liquid Metal Composites Enabled by Adaptive Interfacial Polarization

Chunyan Cao,^{‡a} Xin Huang,^{‡a} Dong Lv,^a Liqing Ai,^a Weilong Chen,^b Changshun Hou,^a

Bo Yi,^a Jingdong Luo,^{*b} Xi Yao^{*ac}

^aDepartment of Biomedical Sciences, City University of Hong Kong, Hong Kong
999077, P. R. China

^bDepartment of Chemistry, City University of Hong Kong, Hong Kong 999077, P. R.
China

^cShenzhen Research Institute of City University of Hong Kong, Shenzhen 518057, P.R.
China

[‡]These authors contributed equally.

Supporting Information

- 1. Supporting Movies**
- 2. Supporting Notes**
- 3. Supporting Figures**

1. Supporting Movies

Movie S1 shows the process of HCl etching procedures at the LM-rich side of composites. During the etching process, tiny shining liquid metal droplets gradually disappeared and the color of the composite changed from silver to dark yellow. Finally, due to high surface tension of liquid metal, these liquid metal droplets were excluded from the polymer matrix and coalesced into large droplets sitting on the surface of the polymer matrix. This movie corresponds to Fig. S6.

Movie S2 shows the shape evolution of an EGaIn droplet sitting on the PVDF-*co*-CTFE polymer substrate under continuous tensile strain. The boundary of EGaIn droplet would extend gradually when the polymer substrate was stretched from 0% to 1400% strains. This movie corresponds to Fig. 2D left in the main text.

Movie S3 shows the shape evolution of an EGaIn droplet sitting on the PVDF-*co*-CTFE polymer substrate under continuous tensile strain after HCl treatment. The EGaIn droplet can't deform with the stretching of the polymer substrate from 0% to 500% strains. This movie corresponds to Fig. 2D right in the main text.

2. Supporting Notes

By folding as-prepared LM-polymer composite and edge-cutting, a capacitor with a three-layered design was obtained. Upon stretching, capacitance changes are mainly caused by the changes of both thickness of dielectric layer and the effective area of the sensor. Thus, the value of capacitance change (ΔC) and the normalized capacitance change (C/C_0) at different strains can be expressed as Eqs. (1) and (2).

$$\Delta C = C - C_0 = \frac{\varepsilon\varepsilon_0 S'}{t_2} - \frac{\varepsilon\varepsilon_0 S}{t_1} = \frac{\varepsilon\varepsilon_0 S't_1 - \varepsilon\varepsilon_0 S t_2}{t_2 t_1} \quad (1)$$

$$\frac{\Delta C}{C} = \frac{S't_1 - S t_2}{S t_2} \quad (2)$$

where C and C_0 are the capacitance before and after stretching, ε_0 is vacuum dielectric permittivity, ε is the dielectric constant of PVDF-co-CTFE and to simplify analysis, we consider it remains constant upon stretching, t_1 and t_2 are the thickness of the capacitor before and after stretching, S and S' are the effective area of the capacitor before and after stretching. The material was non-isotropic and Poisson's ratios in the thickness (V_t) and width (V_w) direction were experimentally determined.¹ As shown in Fig. S21a, thickness of LM-polymer composite decreased from 140 μm to 132 μm , thus $V_t (=0.06)$ could be obtained using Eq. (3). With similar method, $V_w (=0.23)$ could also be obtained using Eq. (4).

$$V_t = \frac{(t_1 - t_2)/t_1}{(L_2 - L_1)/L_1} = \frac{t_1 - t_2}{t_1 \cdot \delta} \quad (3)$$

$$V_w = \frac{(w_1 - w_2)/w_1}{(L_2 - L_1)/L_1} = \frac{w_1 - w_2}{w_1 \cdot \delta} \quad (4)$$

where L_1 , t_1 , w_1 are the length, thickness, width of the specimen before stretching and L_2 , t_2 , w_2 are the length, thickness, width of the specimen after stretching, δ is the strain applied to the samples, respectively.

After stretching from 0% to 100% strains, the corresponding length $L_2 (= L_1 (\delta+1))$, thickness $t_2 (= t_1 - V_1 \delta t_1)$, width $w_2 (= w_1 - V_w \delta w_1)$ of capacitor are obtained. Thus, original effective area before stretching $S (= L_1 \times w_1)$ and after stretching $S' (= L_2 \times w_2)$ could be obtained. The theoretical value of normalized capacitance change (C/C_0) was thus calculated and presented in Fig. S22b. There was a good agreement between the theory and experiment data at strain changes between 0% and 100%.

3. Supporting Figures

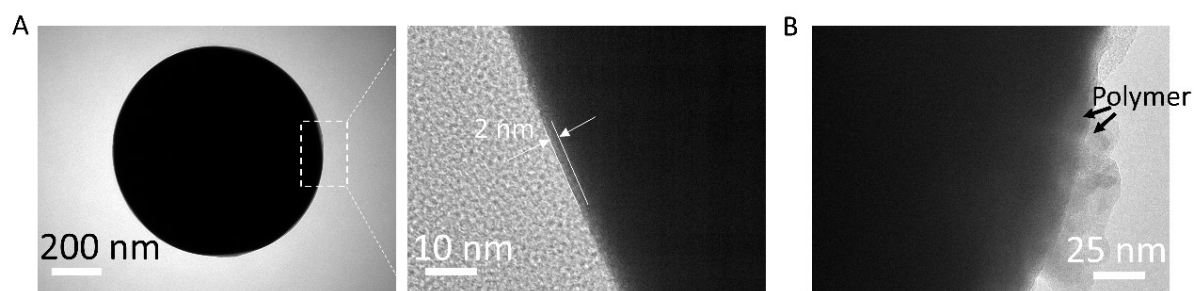


Fig. S1. (A) TEM images of LM droplet produced by sonicating bulk EGaIn in EA solution without the presence of PVDF-*co*-CTFE polymer. Due to its large surface tension, LM droplet displayed spherical shape and an oxide layer (2 nm) was observed on its surface. (B) TEM image of LM droplet produced by sonicating bulk EGaIn in the polymer solution. Wrapping and attachment of a thin polymer layer was observed to its surface.

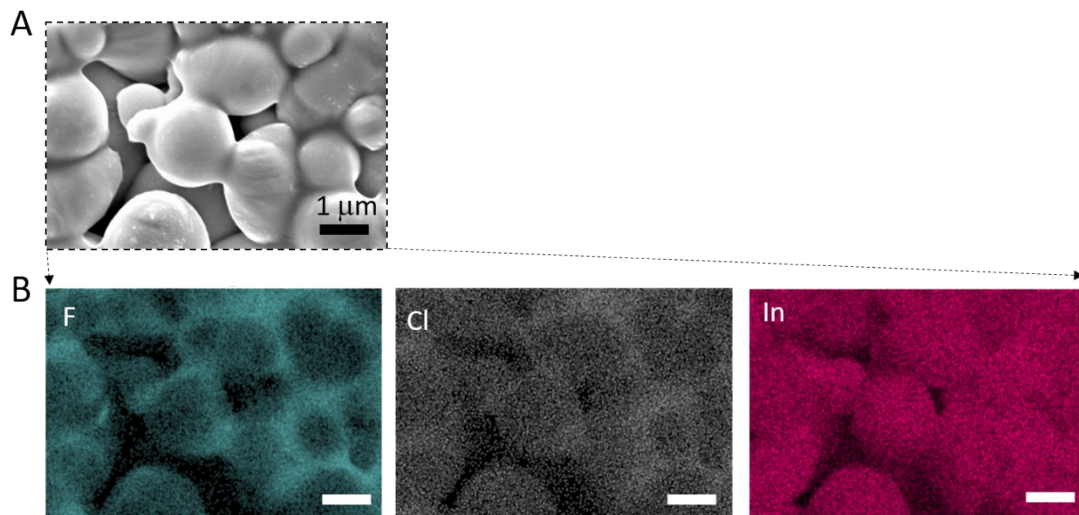


Fig. S2. (A) SEM images of PVDF-*co*-CTFE coated LM droplets and its corresponding EDX element mapping (F, Cl, and In), and other elements was shown in Fig. 1D (C, Ga, O element, sonication time: 20 min). As shown in element mapping, elements of C, F, Cl in PVDF-*co*-CTFE are distributed on the surface of the LM droplets, which indicates that LM droplets are fully encapsulated by the polymer.

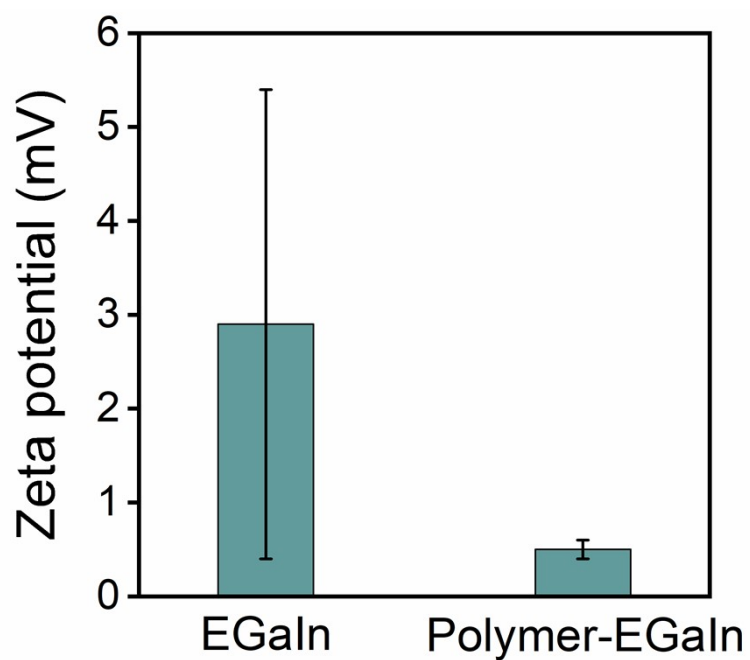


Fig. S3. Comparison on the Zeta potential of the bare EGaIn droplets and the polymer-EGaIn droplets dispersed in water. The concentration of both suspensions was 0.2 wt%. A positive potential of 2.9 ± 2.5 mV was measure for the bare EGaIn droplets, and the value of the polymer-wrapped EGaIn droplets was at 0.5 ± 0.1 mV.

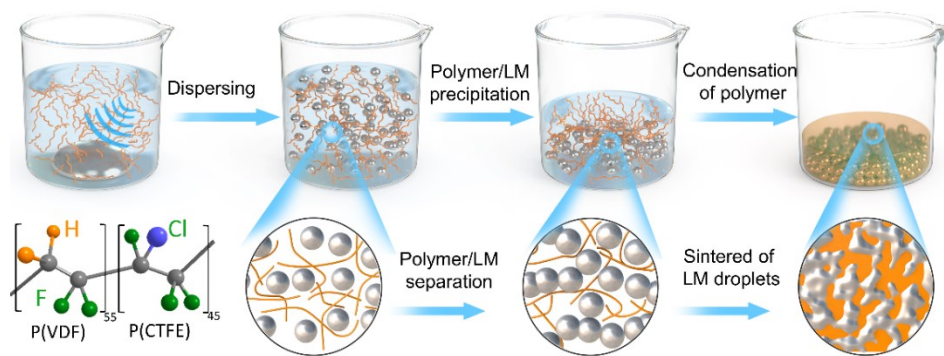


Fig. S4. Schematic illustration of formation process of ultra-stretchable and conductive LM-polymer composite. Under ultrasonic agitation, bulk EGaln was dispersed into micro and nano-scaled droplets. During solvent-evaporation process under ambient condition, the initially homogeneous solution was separated into two layers, the upper layer containing much polymer content and little LM droplets, while the lower layer containing rich LM particles and a certain amount of polymer under the synergistic effect of the sedimentation of LM particles and the precipitation of polymer. With the evaporation of solvent, the sedimented EGaln droplets coalesced into percolated conductive liquid metal network in the bottom side of polymer matrix.

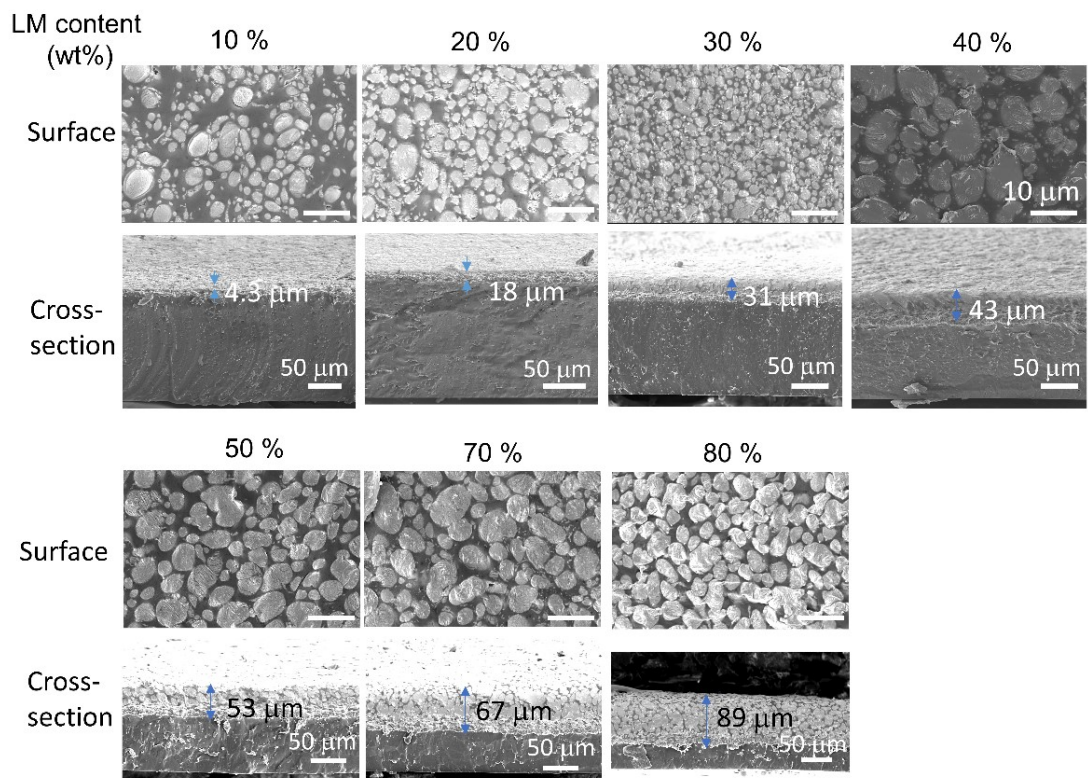


Fig. S5. SEM images of the surface and cross-section of LM-rich sides of composites.

When increasing the mass loading of LM from 10 wt% to 80 wt%, LM-rich sides displayed nearly the same morphology, and the thickness of LM-rich layer increased proportionally from 4.3 μm to 89 μm .

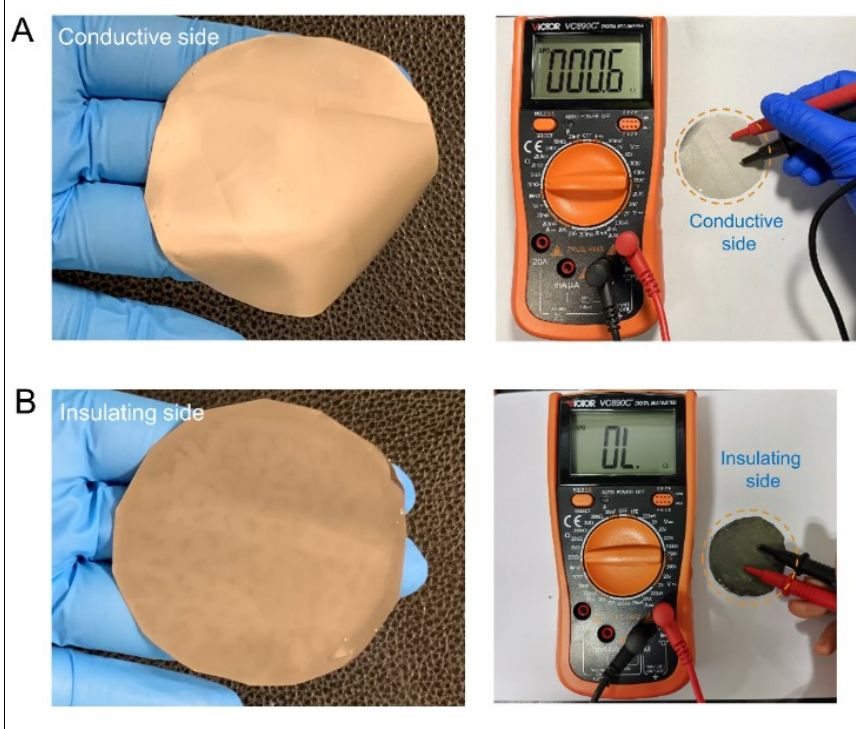


Fig. S6. Representative LM-polymer composite with one side showing high conductivity with resistance of only 0.6 Ω (A), while the other side insulative (B).

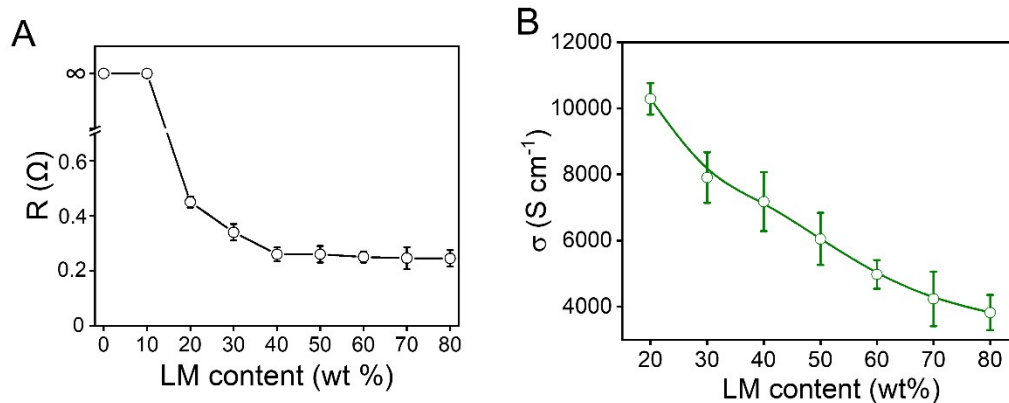


Fig. S7. (A) Resistance and thickness of LM-rich layer for LM-polymer composites with LM mass loading ranged from 0 wt% to 80 wt%. The surface resistance was measured with the surface size of 2.5 cm (length) x 0.3 cm (width). (B) Volume conductivity of LM rich layer of composites with different LM loading ranged from 20 wt% to 80 wt%. It should be noted that there will be some errors between the calculated initial conductivity and actual conductivity because we use the measured surface resistance to calculate the initial volume conductivity.

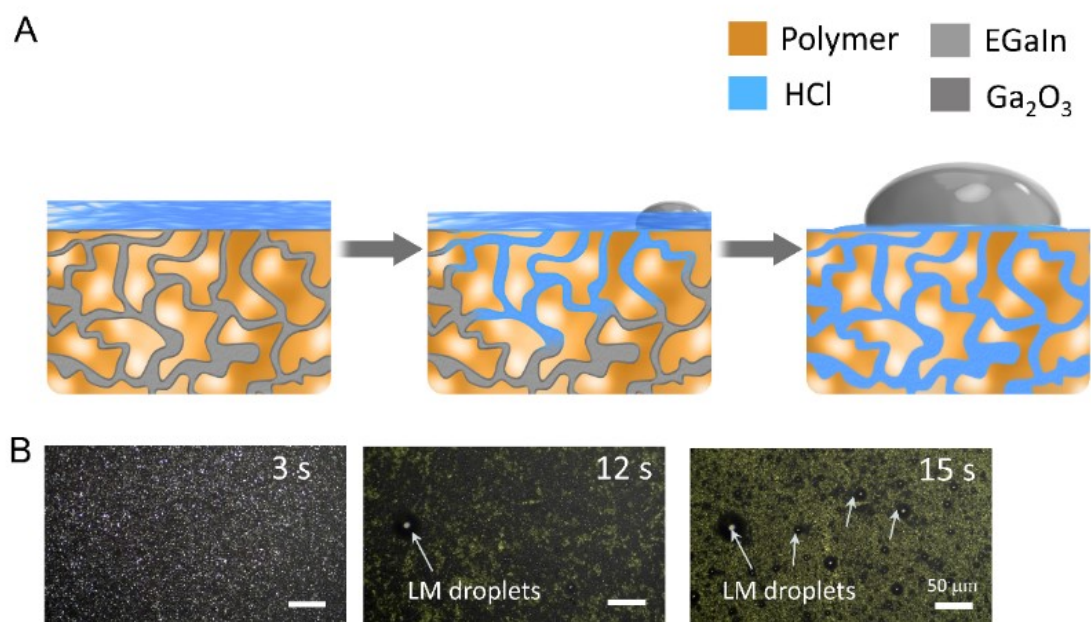


Fig. S8. Acid etching procedures of the LM-polymer composites to help reveal the status of the LM compartments. A) Schematic illustration of using 0.1 M HCl to etch the oxide layer of LMs, after which the compartmented LM would be excluded by capillary force due to its high surface energy. B) Time-lapsed microscopic images showing the etching procedures. With the etching proceeding, the shining liquid metal droplets gradually disappeared and the color of composite changed from silver to dark yellow. Finally, due to high surface tension of liquid metal, the compartmented LM droplets were gradually excluded from the polymer matrix and coalesced into big ones sitting on the surface of the polymer matrix. The detailed etching process was shown in Movie S1.

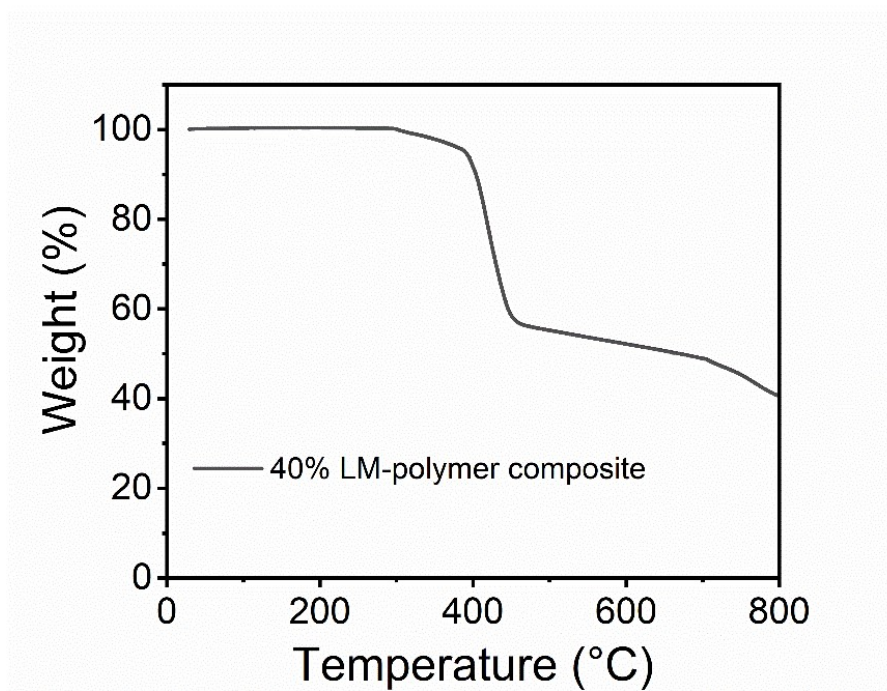


Fig. S9. Representative thermogravimetric analysis (TGA) of the LM-polymer composites with 40 wt% LM loading. It is noted that the onset temperature of thermal decomposition (T_{onset}) of LM-polymer composite was around 300°C.

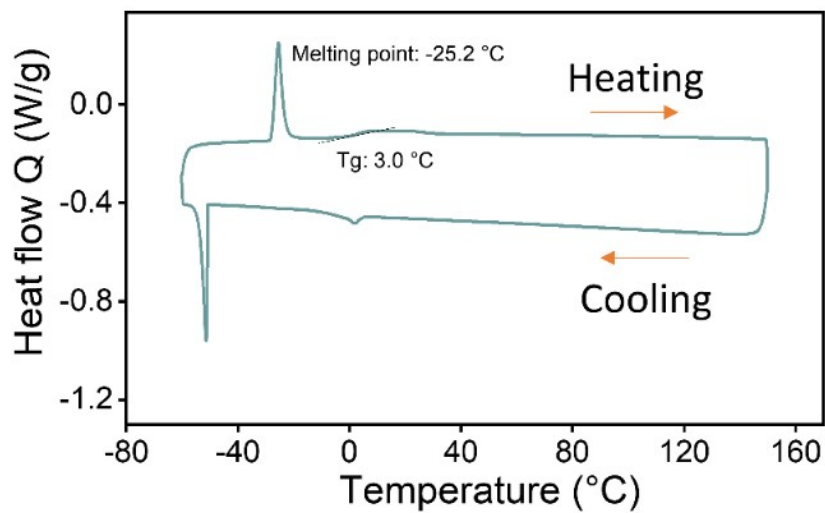


Fig. S10. Representative differential scanning calorimetric (DSC) curves of the LM-polymer composite with first cooling from 150°C to -60°C and subsequent heating from -60°C to 150°C. The T_g of PVDF-*co*-CTFE was measured at 3.0°C, and the melting temperature of micro-nano scaled EGaIn droplets was measured at -25.2°C, which was much lower than bulk phase of EGaIn (15.7°C).

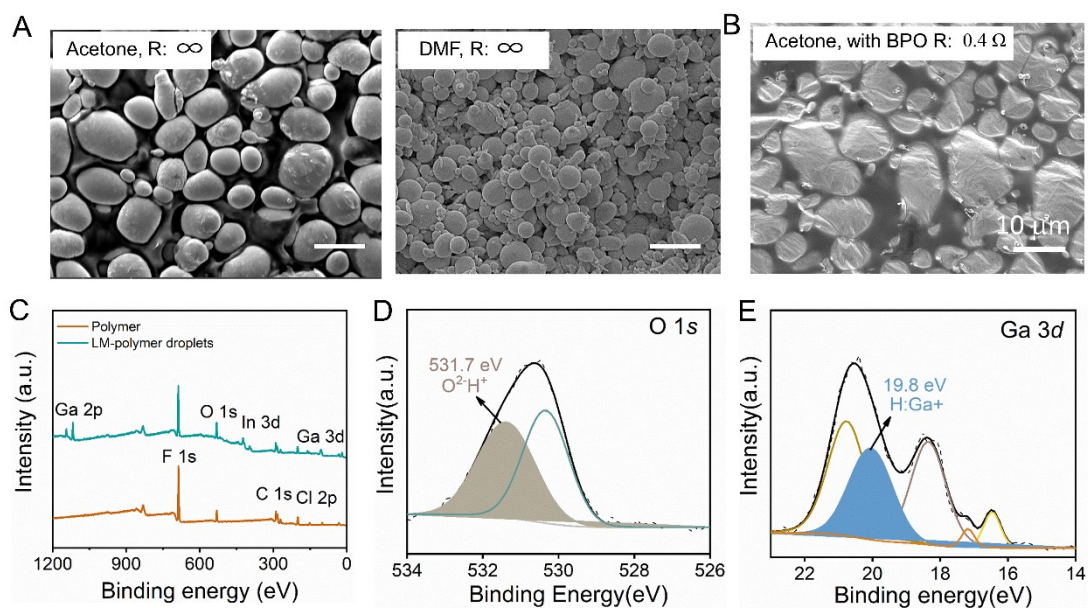


Fig. S11. Influence of solvent on the surface morphology and conductivity of the composites. (A) Representative SEM images of the LM-polymer composite (40 wt% EGaIn) prepared by using acetone and DMF as solvent. The LM-polymer composites displayed immeasurable resistance. (B) Representative SEM image of the LM-polymer composite prepared by introducing a radical initiator (BPO) into the acetone solution. When introducing BPO into these solvents, LM-polymer composite showed high conductivity with resistance of 0.4 Ω because BPO facilitated hydrogen radical production and the H radical activate the oxide layer of LMs. C) Wide XPS spectra of polymer and LM-polymer droplets. Signals from polymer and LM can be detected. D, E) XPS of O 1s and Ga 3d of the LM droplets to reveal the chemical changes of the oxide layer of EGaIn droplets which are caused by the H radical².

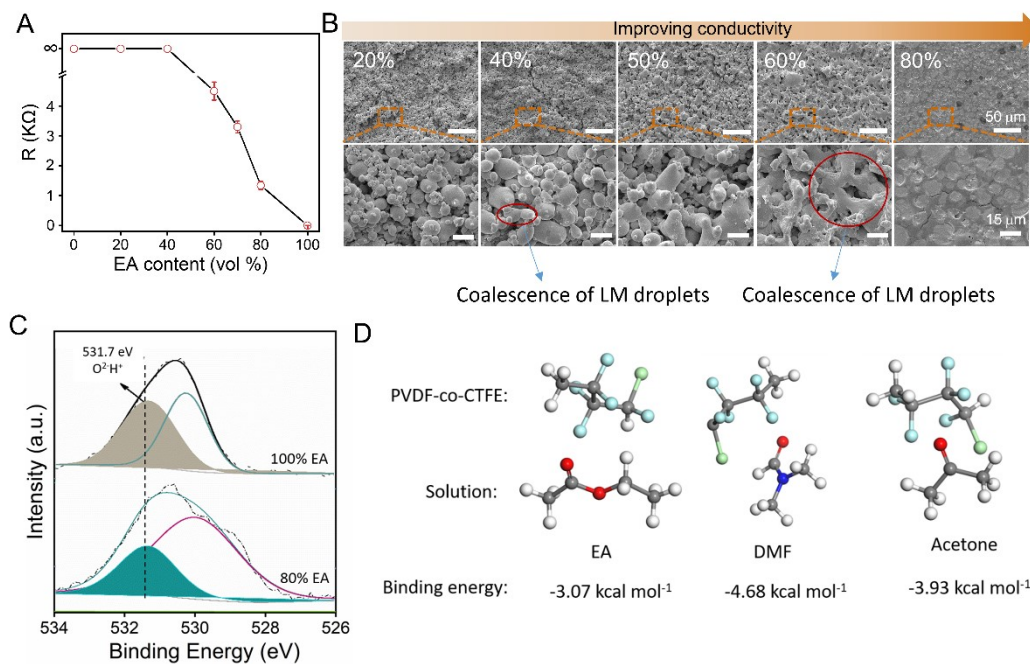


Fig. S12. Tunability of the LM-polymer composites by using mixed solvents. (A) Tuning the resistance of LM-polymer composites by adding more EA to the acetone solution. When EA volume fraction increased from 40% to 100%, the resistance of LM-polymer composites decreased rapidly. (B) Representative SEM images of LM-rich side of composites prepared from the mixed solvents. (C) High-resolution XPS spectra of O1s showing the comparison on chemical changes of the oxide layer of EGaIn droplets when EA content is set at 80% and 100%. (D) Simulations and calculations based on density functional theory (DFT) showing the binding energy between PVDF-co-CTFE and three kind of solvent. It was found that the PVDF-co-CTFE polymer shows the lowest binding energy of $-3.07 \text{ kcal mol}^{-1}$ to EA, compared to DMF ($-4.68 \text{ kcal mol}^{-1}$) and acetone ($-3.93 \text{ kcal mol}^{-1}$). The high binding potential between the polymer and the EA solvent can induce the phase separation of the polymer during the evaporation process may possibly facilitate the coalescence of LM droplets.

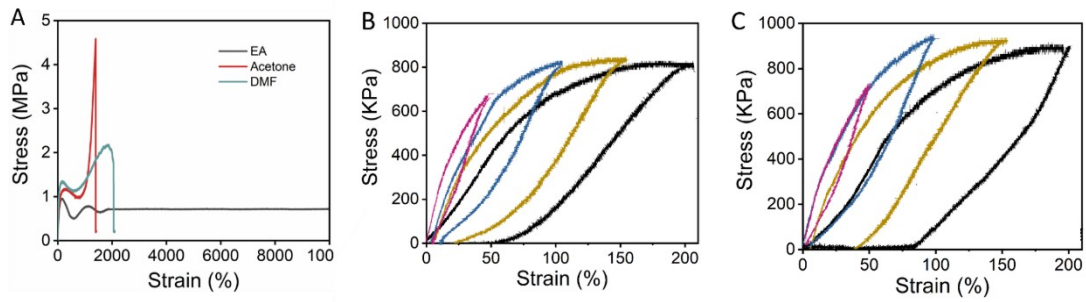


Fig. S13. (A) Influence of solvent selection on the mechanical property of the composites. LM-polymer composites showed confined stretchability (<2100%) when using acetone and DMF as solvent, while displaying ultra-stretchability with strain up to 10000% when using EA as solvent, which is contributed to that appropriate solvent (EA) and doping would optimize the mechanical property³⁻⁵. Consecutive cyclic stretching-releasing curves for LM-composite prepared by using EA (B) and acetone (C) as solvent from 50% to 200%. As displayed in B and C, when the strains were 50%, 100% and 150%, they show nearly same mechanical hysteresis. However, when the strain reaches 200%, LM-composites prepared by using EA as solvent show smaller mechanical hysteresis.

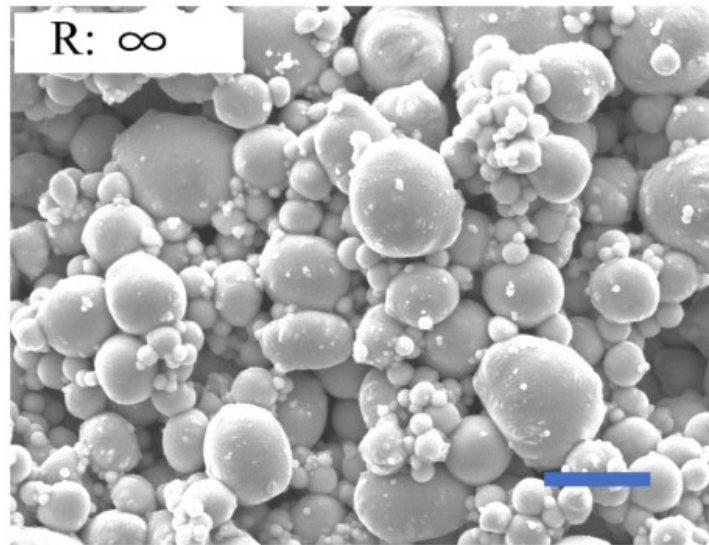


Fig. S14. SEM image of LM droplets and film prepared from suspension without the addition of PVDF-CTFE. The prepared LM film was not conductive. Scar bar is 5 μm .

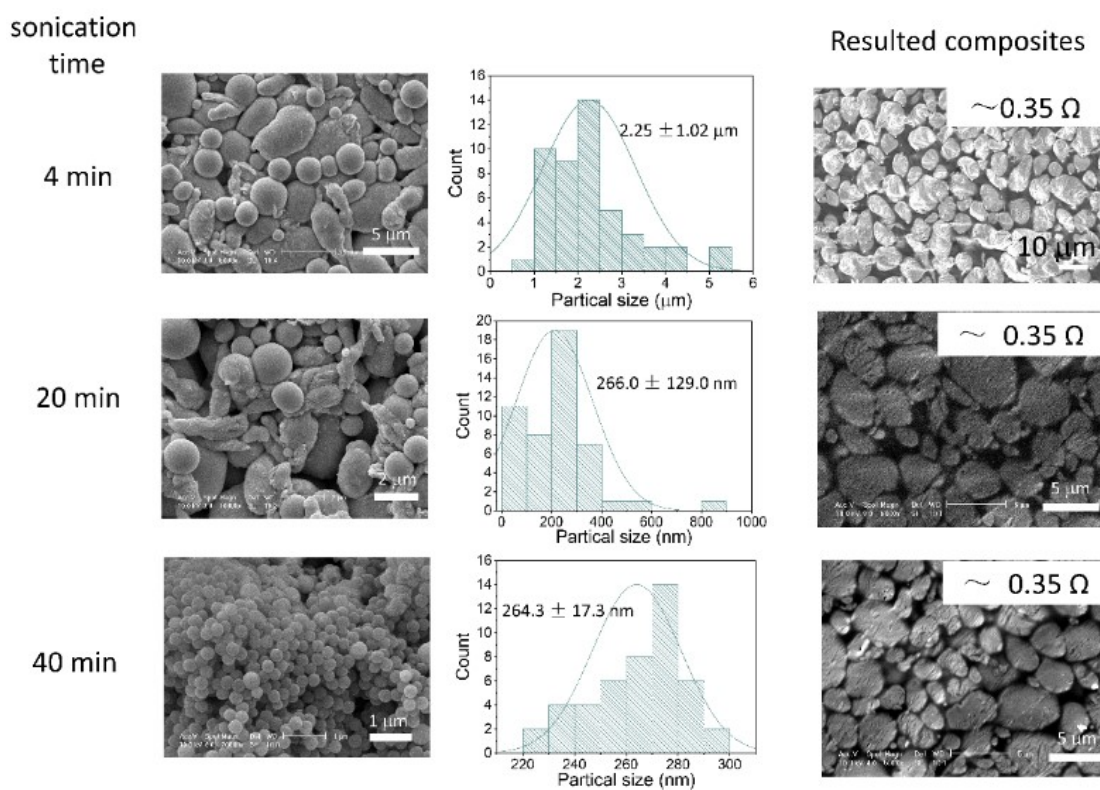


Fig. S15. Influence of solution sonication time on the size distribution of LM droplets and the conductivity of the developed LM-polymer composites. When increasing sonication time from 4 min to 40 min, the average size of LM droplets decreased from 2.25 μm to 264 nm. The diameters of the prepared micro or nanoparticles were obtained by counting more than 100 particles in three to five SEM micrographs for each sample using the ImageJ software. All the as-prepared LM-polymer composites show nearly the same surface resistance of around 0.35 Ω .

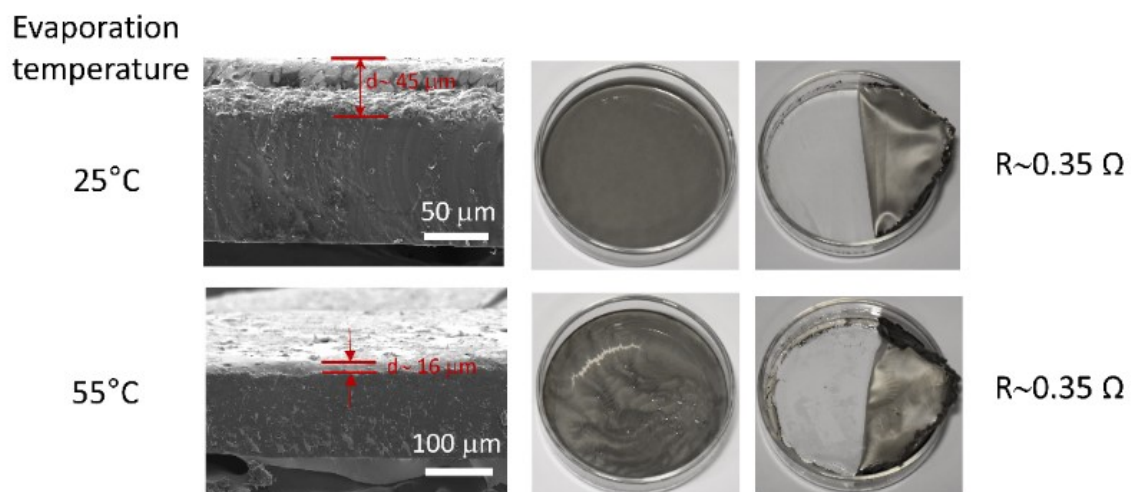


Fig. S16. Influence of evaporation temperature on the conductivity of LM-polymer composites. When LM-polymer suspension was dried at 25°C and 55°C, the obtained LM-polymer composites show different thickness of conductive layer, while the measured surface resistances are nearly the same.

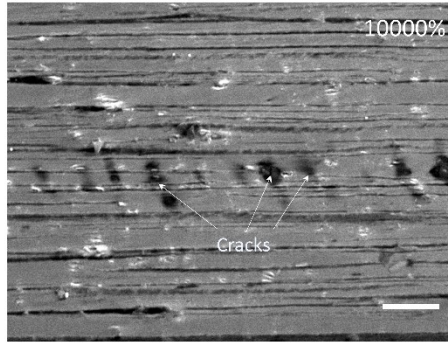


Fig. S17. SEM image of LM-composite (40 % LM) after stretching to strain of 10000%.

Scale bar: 10 μm . After stretching to extremely high strain of 10000%, though some cracks showed, most LMs still maintain continuous states.

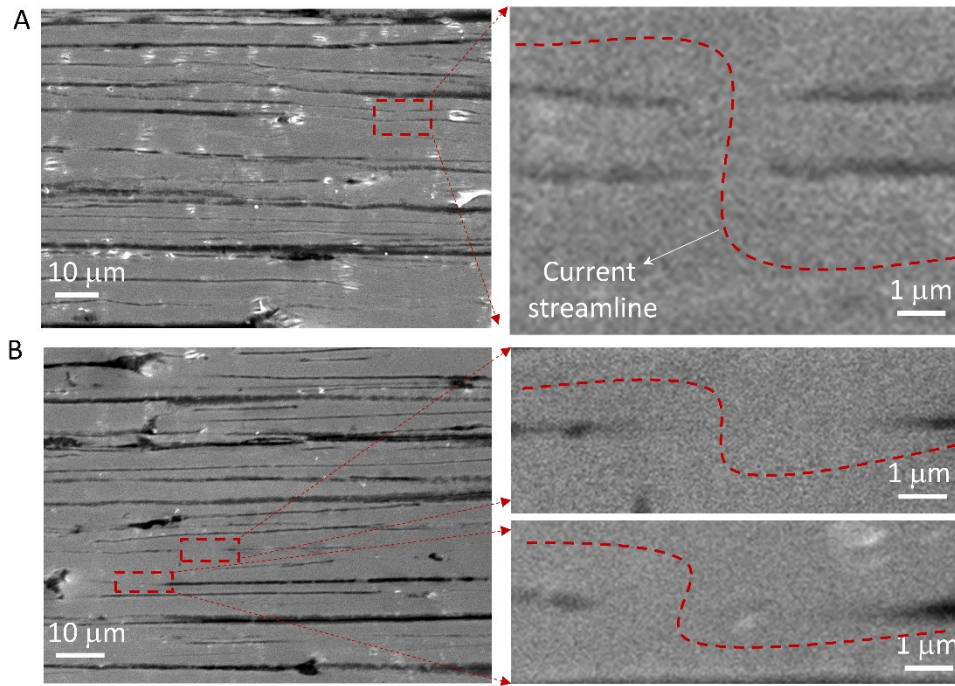


Fig. S18. SEM images of LM-polymer at strain of 3000% (A) and 5000% (B). The liquid metal compartments remain continuous percolation pathway at both strains. As shown in the zoom-in images, the deformed LM compartments break the encapsulation of surrounded PVDF-co-CTFE polymers, flow and connect with each other at the neck positions, resulting in expanded percolation pathway at high strains. The expanded percolation pathway is expected to compensate the changes on the cross-sectional area and the conductive length, and therefore enable the LM-polymer composites to maintain high conductance stability under large strains.

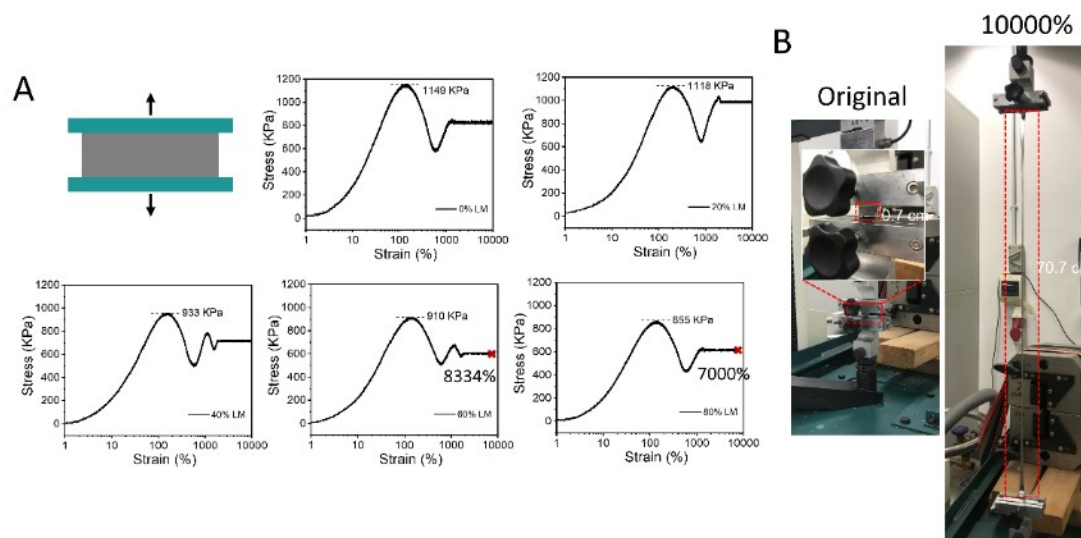


Fig. S19. A) Representative stress-strain curves of LM-polymer composites (sample width, 15 mm; gage length, 7 mm; thickness varies when loading different content of LMs) with different EGaIn loading. LM-polymer composites with LM loading of 10-40 wt% possess a very high stretchability of 10000%. However, the stretchability of LM-polymer composites would decrease to around 7000% when further increasing LM loading to 80 wt%. B) Photographs of LM-polymer composite (40 wt% LM loading) before (0% strain) and after (10000% strain) stretching.

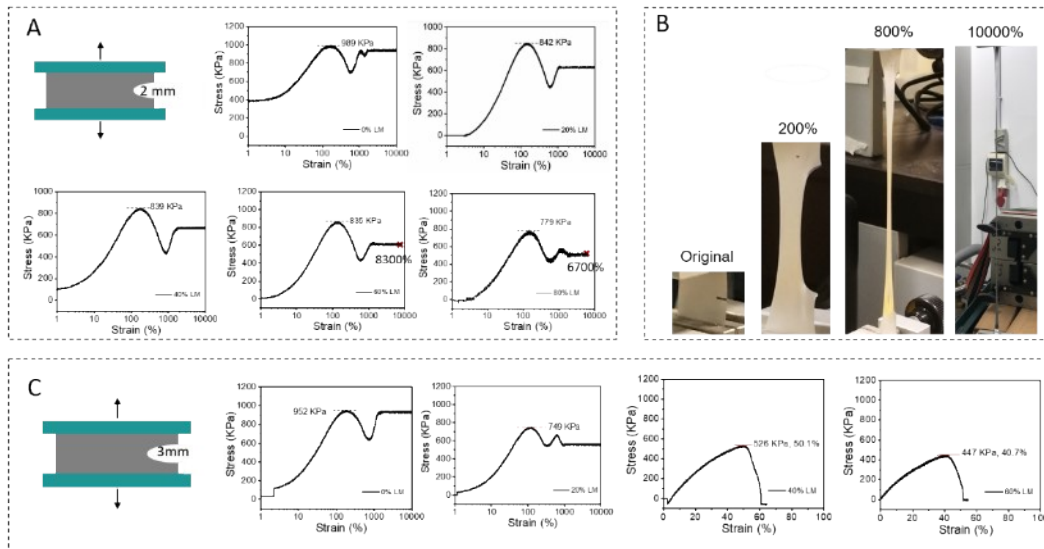


Fig. S20. Notch-insensitivity of the LM-polymer composites with different loading of LMs. (A) Representative stress-strain curves of LM-polymer composites with side notch of 2 mm. With the side notch of 2 mm, LM-polymer composites with LM loading of 10-40 wt% displayed superior notch insensitivity and could still maintain their original stretchability of 10000%. (B) Representative photographs of stretchability of LM-polymer composite (40 wt% LM loading) with side notch of 2 mm, indicating that 2 mm notch would not significantly affect the stretchability of LM-polymer composites. (C) Representative stress-strain curves of LM-polymer composite with side notch of 3 mm, showed that a larger notch would further decrease the mechanical property of LM-polymer composites. Size of all tested samples: width, 10 mm; gage length, 10 mm; thickness varies with different loading of LMs.

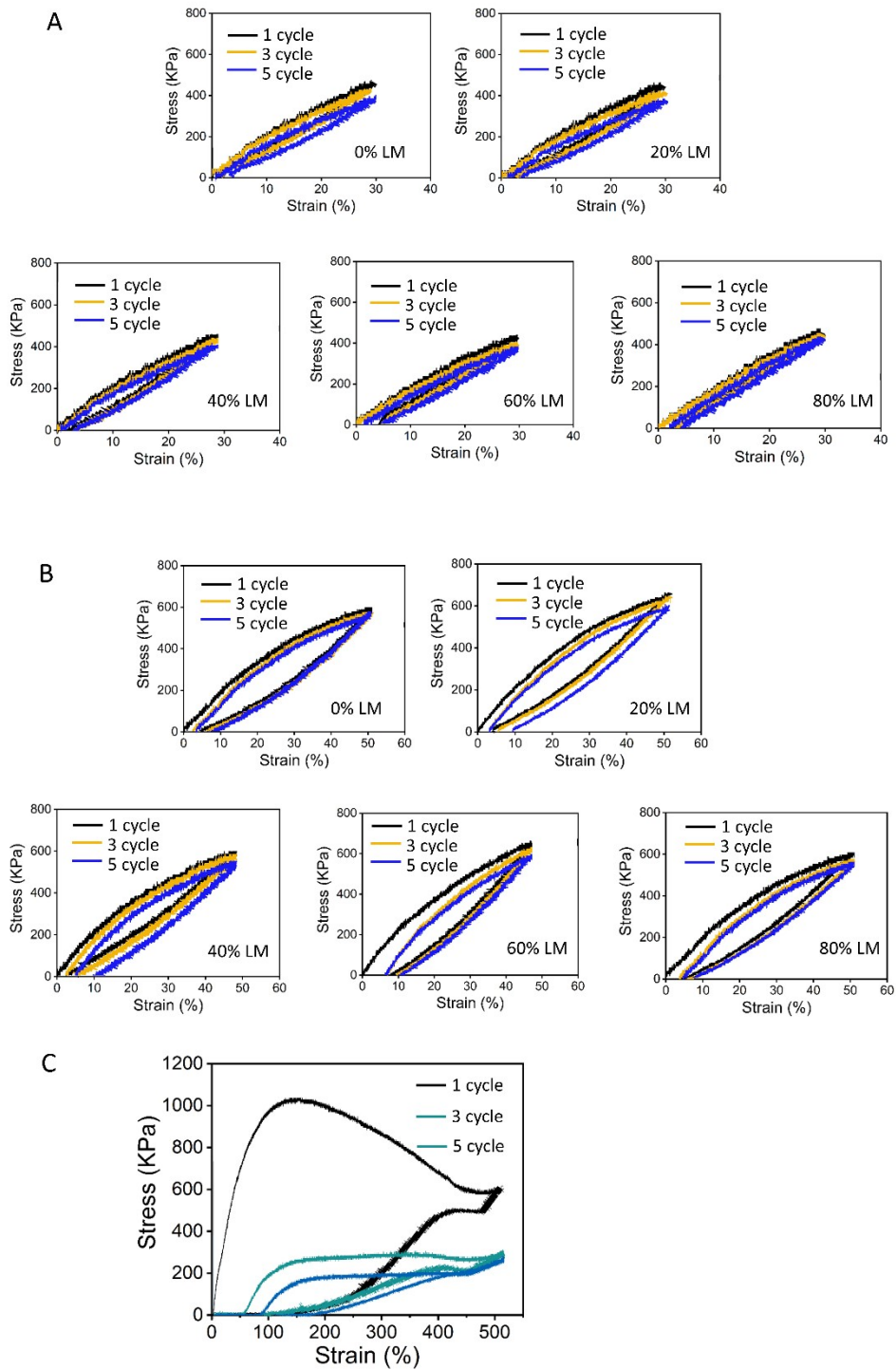


Fig. S21. Representative stress-strain curves of the LM-polymer composites with different LM loading (30% for A and 50% for B) in cyclic stress-strain tests. C) Representative stress-strain curves of the LM-polymer composites with 20% LM loading in cyclic stress-strain tests (500%). All curves showed a small hysteresis at 0%-

30% or 0%-50% strains. Although these composites can be stretched to large strains, they show certain hysteresis because the base polymer is not chemically crosslinked, for example 500%, it displays a relatively large mechanical hysteresis with increased cycles.

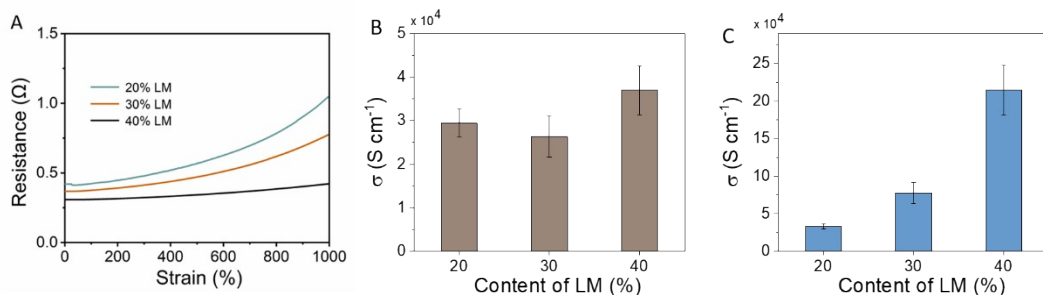


Fig. S22. A) Representative resistance changes of LM-polymer composites with different LM loading of 20, 30 and 40 wt% as a function of applied strains from 0% to 1000%. After stretched to 1000%, all composites display very low resistance (<1.5 Ω). Especially, for LM-polymer composite with 40 wt% LM loading, its resistance is nearly the same as original. B) Considering the volume of the conductive network is constant under stretching, the electrical conductivity after stretching to 1000% (B) and 10000% (C) is calculated by using the equation of $\sigma = L/(RA)$. When stretching to a high strain of 10000%, the calculated conductivity is higher than that of bulk EGaIn (34000 S/cm), especially for composites with 30, 40% LM loading. This phenomenon is possibly attributed to that the large stress caused by stretching destroys some formerly closed cell structure, which makes isolated EGaIn droplets redistribute into the conductive network and increases the volume of conductive network. Therefore, there will be some errors between calculated conductivity and actual conductivity. The width and gage length of original samples are 15 mm and 7 mm, which are the same with the samples used for studying the resistance changes under strain.

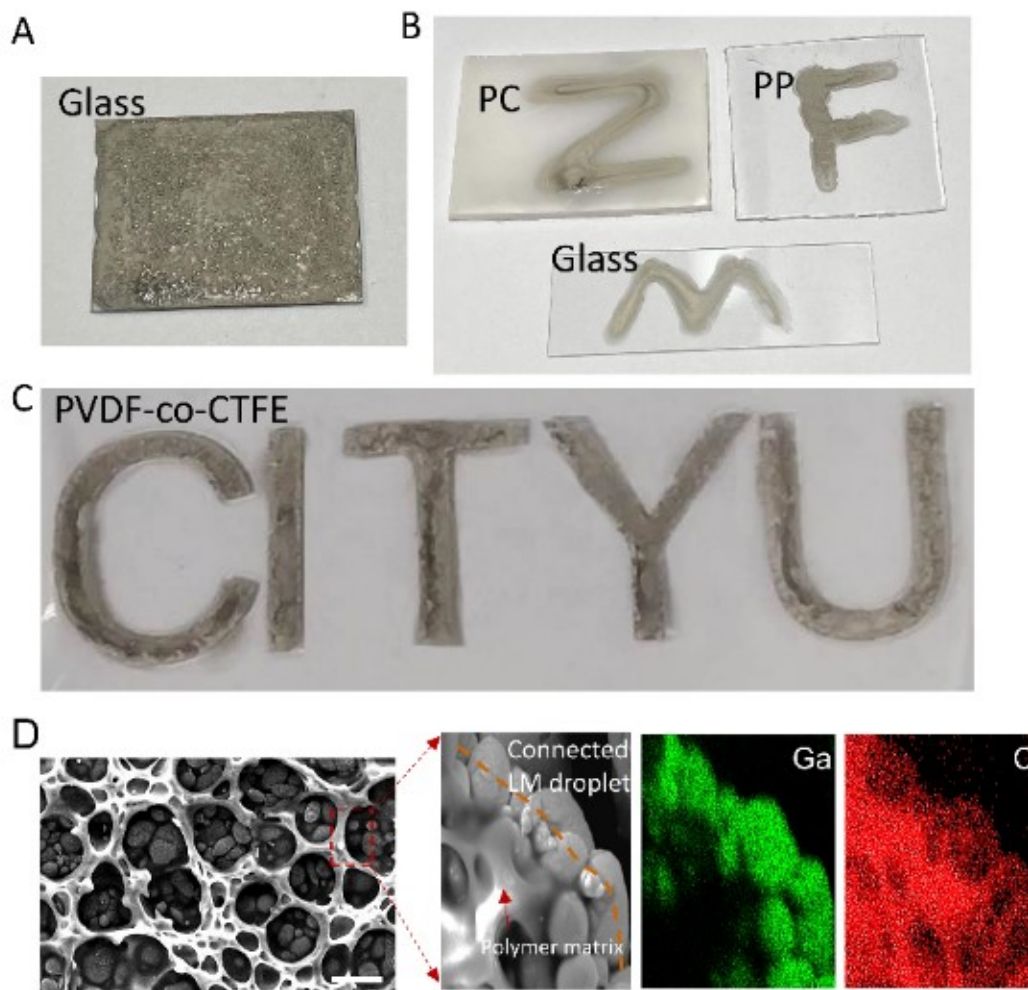


Fig. S23. Using liquid metal/polymer suspension (LM loading: 90 wt%) as conductive ink to obtain conductive patterns on different substrates through (A) drop-casting, (B) hand-writing and (C) screen-printing. (D) SEM image of the conductive pattern on the glass and its corresponding Energy Dispersive X-ray (EDX) mapping, which showed that liquid metal droplets partly coalesced to form conductive pathways surrounded by polymer matrix.

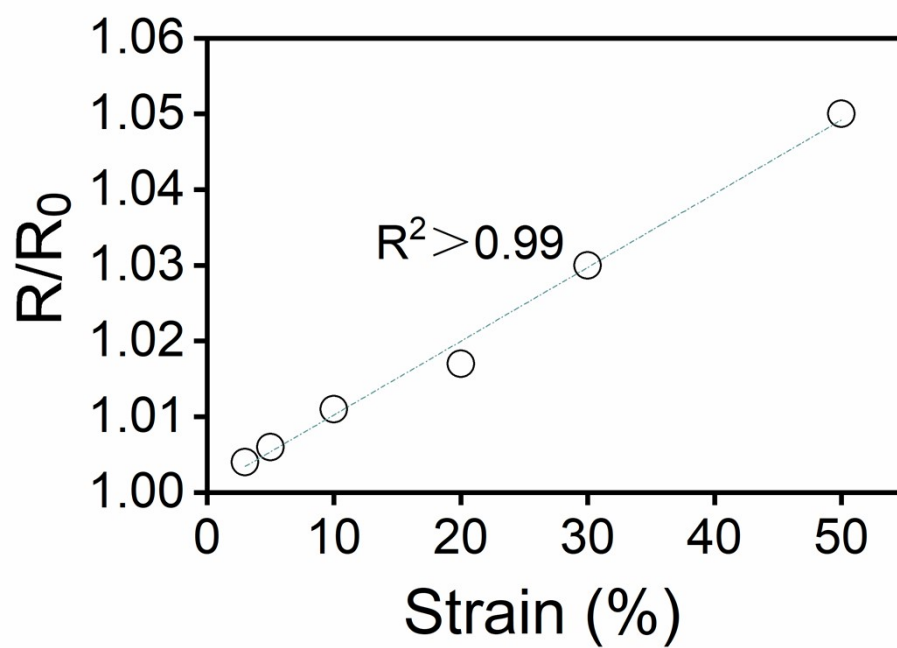


Fig. S24. Resistance change of LM-polymer composite with 20 wt% LM loading. It showed the value of R/R_0 of the composite was in direct proportion to the applied strain with a linearity, $R^2 > 0.99$.

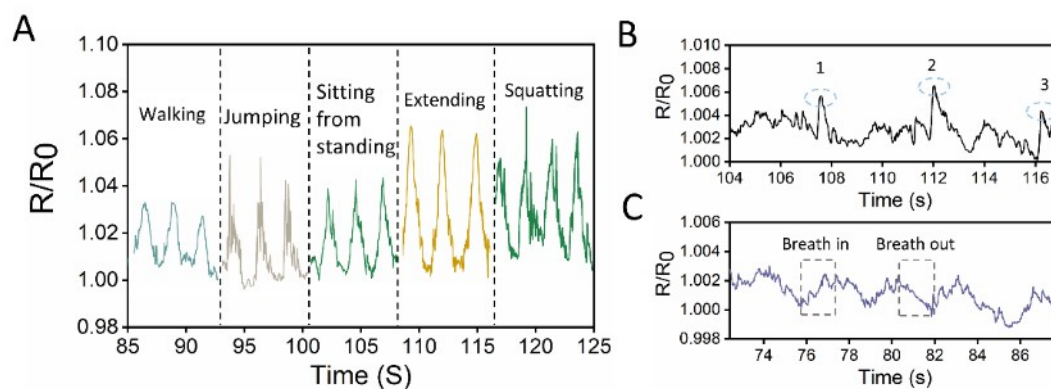


Fig. S25. The conductive LM-polymer composite used as a sensor for human motion detection. (A) The sensor attached onto human leg to detect leg motion, including walking, jumping, sitting from standing, extending, and squatting. (B) Representative resistance changes of the sensor when it was attached to throat for signaling the voice of speaking ‘Speaking’ for three times. (C) Representative resistance changes of the sensor when attaching it to chest and taking several deep breaths.

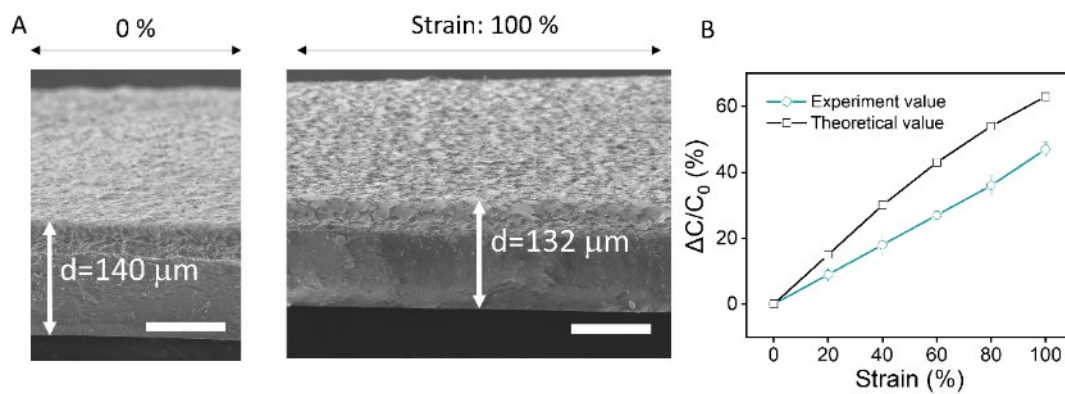


Fig. S26. (A) Representative SEM images of LM-polymer composite (40 wt% LM loading) before and after stretching to 100% strain. Scale bar is $100 \mu\text{m}$. The film thickness was measured accordingly, which will be further used for calculation of capacitance. (B) The theoretical value and the measured (normalized) capacitance were compared at graded strains from 0% to 100%.

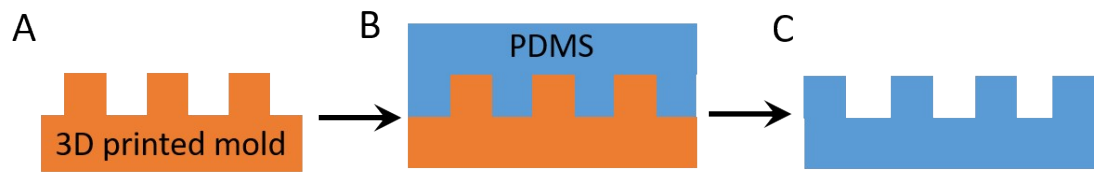


Fig. S27. Fabrication processes of the microstructured dielectric layer. A) A mold with microstructured pillars (diameter and height of pillars were $300\ \mu\text{m}$) was fabricated by 3D printing. B) A mixture of polydimethylsiloxane (PDMS) and curing agent (15:1) was casted into the as-prepared mold. C) After curing, PDMS with embedded micropillars was peeled off from the mold.

4. Supporting Tables

Table S1. Comparison of conductive stability of liquid-metal-based stretchable conductors.

Index	Filler	Matrix/ substrate	strain	R/R ₀ at strain	LM fraction (%)	Ref.
1	EGaIn network	PVDF- <i>co</i> - PCTFE	10000%	20.3	40 wt%	This work
2	EGaIn network	PVDF- <i>co</i> - PCTFE	5000%	7.7	40 wt%	This work
3	EGaIn	PDMS	30%	1.26	100% wt%	(6)
4	EGaIn	HEA	744%	1.85	>99.9 wt%	(7)
5	EGaIn	TPU	500%	3	~54 wt%	(8)
6	3-D EGaIn network	PDMS	200%	/	/	(9)
7	Ni flakes and EGaIn particles	CPU	700%	17.7	28 wt%	(10)
8	3-D EGaIn network	PDMS	50%	1.5	/	(11)
9	Galistan particles	PDMS	133%	/	87 wt%	(12)
10	EGaIn bulk core	SEBS	750%	85	/	(13)
11	EGaIn and Ag NPs	PDMS	80%	1.3	/	(14)
12	EGaIn and Ag flakes	EVA	1000%	8	66.7 wt%	(15)
13	EGaIn particles	PDMS	50%	/	50 vol%	(16)
14	EGaIn particles	Sulfur	~10%	/	30 vol%	(17)
15	EGaIn particles	PDMS	500%	~1	<70 vol%	(18)
16	Fe-GaIn	PVA	300%	18	15 vol%	(19)
17	3-D EGaIn network	PDMS	400%	/	/	(20)
18	EGaIn	PMA-PU	523%	~800	/	(21)

19	EGaIn-Cu	cotton fabrics	75%	2.5	/	(22)
20	EGaIn-Cu	PU	200%	~7	/	(23)
21	EGaIn-Ag flakes	PUA	2500%	10	50 wt%	(24)
22	EGaInNi	polyacrylate	300%	~10	/	(25)
23	EGaIn	PDMS	400%	~3	/	(26)
24	EGaIn	PHEA- <i>co</i> - PEGDA hydrogel	1500%	2.3	/	(27)
25	biphasic Ga-In	VHB	1000%	5	/	(28)
26	EGaIn	SBS	1800%	1.36	/	(29)

References

1. K. Y. Chun, Y. Oh, J. Rho, J. H. Ahn, Y. J. Kim, H. R. Choi and S. Baik, *Nat. Nanotechnol.* 2010, **5**, 853-857.
2. S. Veerapandian, W. Jang, J. B. Seol, H. Wang, M. Kong, K. Thiyagarajan, J. Kwak, G. Park, G. Lee, W. Suh, I. You, M. E. Kılıç, A. Giri, L. Beccai, A. Soon and U. Jeong, *Nat. Mater.* 2021, **20**, 533.
3. T. Zuo, J. Li, Z. Gao, Y. Wu, L. Zhang, B. Da, X. Zhao and L. Xiao, *Mater. Today Commun.* 2020, **23**, 100907.
4. Z. Sang, H. Guo, K. Ke and I. Manas-Zloczower, *Macromol. Mater. Eng.* 2019, **304**, 1900278.
5. P. Baek, N. Aydemir, Y. An, E. W. C. Chan, A. Sokolova, A. Nelson, J. P. Mata, D. McGillivray, D. Barker and J. Travas-Sejdic, *Chem. Mater.* 2017, **29**, 8850-8858
6. B. Deng and G. J. Cheng, *Adv. Mater.* 2019, **31**, 1807811.
7. C. J. Thrasher, Z. J. Farrell, N. J. Morris, C. L. Willey and C. E. Tabor, *Adv. Mater.* 2019, **31**, 1903864.
8. R. Zheng, Y. Wu, Y. Xu, S. Liu, H. Liu, P. Wang, Z. Deng, S. Chen and L. Liu, *Mater. Lett.* 2019, **235**, 133-136.
9. J. Park, S. Wang, M. Li, C. Ahn, J. K. Hyun, D. S. Kim, D. K. Kim, J. A. Rogers, Y. Huang and S. Jeon, *Nat. Commun.* 2012, **3**, 916.
10. S. Park, G. Thangavel, K. Parida, S. Li and P. S. Lee, *Adv. Mater.* 2019, **31**, 1805536.
11. S. Liang, Y. Li, Y. Chen, J. Yang, T. Zhu, D. Zhu, C. He, Y. Liu, S. Handschuh-Wang and X. Zhou, *J. Mater. Chem. C* 2017, **5**, 1586-1590.
12. A. Fassler and C. Majidi, *Adv. Mater.* 2015, **27**, 1928-1932.
13. S. Zhu, J.-H. So, R. Mays, S. Desai, W. R. Barnes, B. Pourdeyhimi and M. D. Dickey, *Adv. Funct. Mater.* 2013, **23**, 2308-2314.
14. M. Tavakoli, M. H. Malakooti, H. Paisana, Y. Ohm, D. G. Marques, P. Alhais Lopes, A. P. Piedade, A. T. de Almeida and C. Majidi, *Adv. Mater.* 2018, **30**, 1801852.
15. J. Wang, G. Cai, S. Li, D. Gao, J. Xiong and P. S. Lee, *Adv. Mater.* 2018, **30**, 1706157.
16. E. J. Markvicka, M. D. Bartlett, X. Huang and C. Majidi, *Nat. Mater.* 2018, **17**, 618-624.
17. Y. Xin, H. Peng, J. Xu and J. Zhang, *Adv. Funct. Mater.* 2019, **29**, 1808989.
18. H. Wang, Y. Yao, Z. He, W. Rao, L. Hu, S. Chen, J. Lin, J. Gao, P. Zhang, X. Sun, X. Wang, Y. Cui, Q. Wang, S. Dong, G. Chen and J. Liu, *Adv. Mater.* 2019, **31**, e1901337.
19. R. Guo, X. Sun, B. Yuan, H. Wang and J. Liu, *Adv. Sci.* 2019, **6**, 1901478.
20. B. Yao, W. Hong, T. Chen, Z. Han, X. Xu, R. Hu, J. Hao, C. Li, H. Li, S. E. Perini, M. T. Lanagan, S. Zhang, Q. Wang and H. Wang, *Adv. Mater.* 2020, **32**, 1907499.
21. G. Chen, H. Wang, R. Guo, M. Duan, Y. Zhang and J. Liu, *ACS Appl. Mater. Interfaces* 2020, **12**, 6112-6118.

22. R. Guo, H. Wang, X. Sun, S. Yao, H. Chang, H. Wang, J. Liu and Y. Zhang, *ACS Appl. Mater. Interfaces* 2019, **11**, 30019-30027.
23. Y. Yu, J. Guo, B. Ma, D. Zhang and Y. Zhao, *Sci. Bull.* 2020, **65**, 1752-1759.
24. K. Parida, G. Thangavel, G. Cai, X. Zhou, S. Park, J. Xiong and P. S. Lee, *Nat. Commun.* 2019, **10**, 2158.
25. Y. Wu, Z. Deng, Z. Peng, R. Zheng, S. Liu, S. Xing, J. Li, D. Huang and L. Liu, *Adv. Funct. Mater.* 2019, **29**, 1903840.
26. B. Ma, C. Xu, J. Chi, J. Chen, C. Zhao and H. Liu, *Adv. Funct. Mater.* 2019, **29**, 1901370.
27. J. E. Park, H. S. Kang, M. Koo and C. Park, *Adv. Mater.* 2020, **32**, 2002178.
28. S. Liu, D. S. Shah and R. Kramer-Bottiglio, *Nat. Mater.* 2021, **20**, 851-858.
29. Z. Ma, Q. Huang, Q. Xu, Q. Zhuang, X. Zhao, Y. Yang, H. Qiu, Z. Yang, C. Wang, Y. Chai and Z. Zheng, *Nat. Mater.* 2021, **20**, 859-868.